Dynamics of a spherical colloid at a liquid interface: A lattice Boltzmann study

Harinadha Gidituri, Alois Würger, Kevin Stratford, Juho Lintuvuori

Dynamics of a spherical colloid at a liquid interface: a lattice Boltzmann study

Harinadha Gidituri,[1] Alois Würger,[1, a)] Kevin Stratford,[2] and Juho S. Lintuvuori[1, b)]
[1)] *Univ. Bordeaux, CNRS, LOMA, UMR 5798, F-33405 Talence, France*
[2)] *EPCC, University of Edinburgh, EH8 9BT, Edinburgh, United Kingdom*

(Dated: 8 April 2021)

We study the dynamics of a spherical colloidal particle pulled along fluid-fluid interface using lattice Boltzmann (LB) simulations. We consider an interface with a finite width and include both the effects of the thermodynamics of the interface and the particle wetting, characterised by the contact angle θ between the particle surface and the interface, in addition to the viscosity ratio λ between the two fluids. We characterise the particle dynamics by applying a constant pulling force along the interface and measure both the translational and the rotational dynamics as a function of the contact angle and the viscosity ratio. We observe that the hydrodynamic drag is reduced and the particle rotation is increased when the particle resides more in the low viscosity fluid, in agreement with previous hydrodynamic theories. We also present a case where the particle rotation is suppressed. Then, the drag is observed to increase as compared to the situation where rotation is allowed, while the general behaviour of reducing drag while the particle thermodynamically prefers the lower viscosity fluid, is retained.

Keywords: Colloidal particle, contact angle,wetting, Lattice-Boltzmann Method (LBM), drag force, torque

I. Introduction

Colloidal particles trapped at fluid-fluid interface can be seen in plethora of systems, such as stabilization of emulsions[1–3], foams[4,5], bijels[6–9] and liquid marbles[10,11]. Colloidal particles are spontaneously adsorbed on to the fluid-fluid interface and energetics govern the state of the system to reach a minimum energy as first observed by Ramsden[12] and Pickering[13]. The dynamics of a spherical particle trapped at an interface between two fluids or fluid and gas is a widely studied problem both experimentally[14–18] and theoretically[19–25], due to its importance in various chemical, oil and mineral flotation industries. The hydrodynamic drag of the colloid along the interface depends crucially on the viscosity difference between the two fluids and the particle wetting. In several experiments it has been observed that the hydrodynamic drag decreases when a larger portion of the particle is immersed in the low viscosity fluid or gas[14–18]. This behavior has been reproduced in theoretical studies, where the drag force is calculated using Stokes hydrodynamics with various boundary conditions, including the presence of shear and dilational surface viscosities[19], a finite ratio of bulk viscosities[20], or a solid or membrane boundary on the opposite surface of a thin film[22].

In most previous theoretical approaches[19–22], the particle dynamics was studied from a purely hydrodynamic perspective, with the boundary conditions implemented through an infinitely thin interface. The thermodynamics of the interface was reduced to the definition of a contact angle. A very recent study concerning the effects of buoyancy-driven interface deformations on the effective drag coefficient[23], accounted for the thermodynamics of the interface between the two fluids in 2-dimensions.

In this paper we consider the hydrodynamics of an interface particle, and take into account both the thermodynamics of a finite-thickness interface and particle wetting. Using lattice Boltzmann simulations, we explicitly solve the coupled Navier-Stokes and Cahn-Hilliard equations for the binary fluid with surface wettable colloidal particles[26] in 3-dimensions. The hydrodynamic boundary conditions at the interface arise from the thermodynamic stress. To simulate the particle dynamics, we set the particle wetting properties, the interfacial tension and the viscosities of the two fluids. The particle is pulled along the interface by a constant force F simulating an active microrheology experiment. The translational and rotational dynamics of the particle are governed by the thermo-hydrodynamic stress integrated over the particle surface as a response to the applied force. We consider two situations: In the first one, the particle rotates due to the torque resulting from the unlike traction exerted on the upper and lower hemispheres, which occurs for a free interface and a perfectly spherical particle. In the second case, particle rotation is inhibited, which in physical terms may occur for surfactant laden interfaces or for contact-line pinning on the particle surface.

II. Methods and simulation details

A. Binary fluid model

To model the thermodynamics of the interface, we consider a phase separating binary fluid characterised by a composition $\phi(\mathbf{r})$. The phase behavior is described by a

[a)] Electronic mail: alois.wurger@u-bordeaux.fr
[b)] Electronic mail: juho.lintuvuori@u-bordeaux.fr

Ginzburg-Landau free energy functional[26],

$$G[\phi] = \int dV \left(-\frac{A}{2}\phi^2 + \frac{B}{4}\phi^4 + \frac{\kappa}{2}|\nabla\phi|^2 \right), \quad (1)$$

where A, B and κ are constants. The first two terms describe the bulk properties; the choice of $A = B > 0$ corresponds to a phase separated state with equilibrium compositions $\phi^* = \pm A/B = \pm 1$. The third term represents the energy cost of interfaces. The interfacial thickness χ and tension σ are related to the above parameters,

$$\chi = \sqrt{\frac{2\kappa}{|A|}}, \quad \sigma = \sqrt{\frac{8\kappa|A|^3}{9B^2}}. \quad (2)$$

At the equilibrium, the composition profile is given by

$$\phi/\phi^* = \tanh(z/\chi), \quad (3)$$

where z is the coordinate normal to the interface, and the location of an idealized interface can be identified by $\phi = 0$.

The temporal evolution of phase field variable ϕ is governed by a Cahn-Hilliard advection-diffusion equation,

$$\partial_t\phi + \mathbf{v}\cdot\nabla\phi = M\nabla^2\mu, \quad (4)$$

where $\mathbf{v}$ is the fluid velocity, M is the mobility and μ is the chemical potential derived from the free energy functional in Eq. 1 by $\mu = \frac{\delta G}{\delta\phi} = A\phi + B\phi^3 - \kappa|\nabla^2\phi|$. The fluid velocity is obtained by solving incompressible Navier-Stokes equation,

$$\rho\partial_t\mathbf{v} + \mathbf{v}\cdot\nabla\mathbf{v} = \eta\nabla^2\mathbf{v} - \nabla P - \phi\nabla\mu, \quad (5)$$

where the gradient of the hydrodynamic pressure P is supplemented by the thermodynamic force $\phi\nabla\mu$.

Binary fluids with different wetting preferences towards a solid surface can be modeled by including an additional surface free energy $G_s(\phi_s)$ to Eq. 1, where ϕ_s is the order parameter in contact with the surface. The total free energy of the combined system (binary fluid + colloid) is given by[27]

$$G_{total} = G[\phi] + \int G_s(\phi_s)ds, \quad (6)$$

with a surface contribution

$$G_s = \frac{C}{2}\phi_s^2 + H\phi_s. \quad (7)$$

The equilibrium order parameter profile ϕ_s and the boundary condition at the solid surface

$$\frac{dG_s}{d\phi_s} = \kappa|\nabla\phi\cdot\mathbf{n}| \quad (8)$$

where $\mathbf{n}$ is the particle surface normal, can be obtained from the functional minimization of the total free energy (Eq. 6)[27].

Different wetting behaviors can modeled by tuning of C and H values in Eq. 7. A finite value of C should be considered for systems with a wetting phase transition. In the current study, we considered $C = 0$ in all cases. The two fluid-solid interfacial tensions can be readily be modified by changing the parameter H. For $H = 0$ the surface will have an equal affinity towards both fluids, corresponding to a neutrally wetting colloid ($\theta = 90°$). A non-zero value of H causes an asymmetry which results in a deviation of the contact angle from 90°.

B. Simulation details

The simulations were carried out using a hybrid method, where the evolution of the order parameter was solved using finite difference and the flow field $\mathbf{v}(\mathbf{r})$, arising from the continuity and Navier-Stokes equations, using lattice Boltzmann[28]. The colloids were modelled as spherical particles with a radius R lattice sites. The no-slip boundary condition at the particle surface was realised by a standard method bounce-back on links method. [29,30], and the boundary condition for ϕ was solved numerically[27].

We use a 3-dimensional simulation domain consisting of $128 \times 128 \times 128$ lattice sites with periodic boundary conditions in all directions.

The simulation parameters below are given in lattice units, where the lattice spacing, time step and density are fixed to unity: $\Delta x = 1$, $\Delta t = 1$ and $\rho = 1$, as customary in LB simulations. The size of the colloid is fixed at $R = 12\Delta x$. The validation of the domain and colloid sizes are presented in the appendix.

The viscosity of the $\phi = +1$ fluid was fixed $\eta_1 = 0.625$ throughout the paper. The viscosity ratio ($\lambda = \eta_2/\eta_1$) is varied by changing the viscosity η_2 of the $\phi = -1$ fluid. To have a continuous viscosity across the interface, a composition dependant viscosity $\eta(\phi)$ following an Arrhenius relation[31],

$$\eta(r) = \eta_2^{\frac{1-\phi}{2}}\eta_1^{\frac{1+\phi}{2}} \quad (9)$$

was used.

The densities of both of the fluids and the colloids were fixed for a constant value of 1.0. For the binary fluid $A = B = 0.00258$, surface penalty $\kappa = 0.004$ and mobility $M = 4.0$ were used. Using the parameters above and Eq. 2, we get an interfacial width $\chi \approx 1.76$ and interfacial tension $\sigma \approx 0.003$ in lattice units.

We consider both freely rotating particles, and particles without rotational motion. To inhibit the rotation, a director $\hat{\mathbf{s}}$ is assigned on the particle and strong magnetic field $\mathbf{B}_0$ is applied to align the particle director $\hat{\mathbf{s}}$ along the applied force $\mathbf{F}$. The resulting torque $\mathbf{T} = \mathbf{B}_0 \times \hat{\mathbf{s}}$ inhibits the rotational motion of the particle.

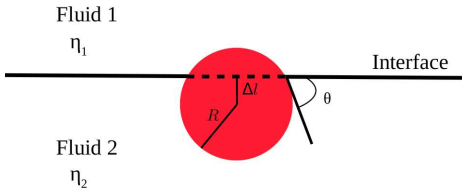

FIG. 1. Schematic representation of a colloid particle with radius R at fluid-fluid interface with two different viscosities η_1 and η_2 respectively. The contact angle (θ) is defined as the angle measured between the tangent at the colloid surface and fluid-fluid interface.

C. Particle contact angle

We study the dynamics of a colloidal particle at a fluid-fluid interface. A spherical colloidal particle of radius R is placed at an interface between two fluids with different viscosities $\eta_1 \geq \eta_2$ (Fig. 1). Depending on the surface wetting, the particle adopts a contact angle θ in equilibrium which can be measured using a relation

$$\cos\theta = \frac{\Delta l}{R} \tag{10}$$

where Δl is the difference between interface position and center of the colloid (Fig. 1).

In the simulations, the contact angle can be tuned by varying the free energy parameters and follows theoretically[27]

$$\cos\theta = \frac{1}{2}[-(1-h)^{\frac{3}{2}} + (1+h)^{\frac{3}{2}}] \tag{11}$$

where the wetting parameter h is given by,

$$h = \frac{H}{\sqrt{\kappa B}}. \tag{12}$$

D. Non-dimensional numbers

The hydrodynamic non-dimensional numbers describing the interface deformation and flow behavior are the capillary and Reynolds numbers, respectively

$$\mathrm{Ca} = \frac{\eta_1 V}{\sigma} \tag{13}$$

$$\mathrm{Re} = \frac{\rho R V}{\eta_1}, \tag{14}$$

where V is the steady state particle velocity, and the viscosity η_1 of the fluid $\phi = +1$ was used in the calculation of both Re and Ca. Using the simulations parameters, we recover Re $\sim \mathcal{O}(10^{-3} - 10^{-4})$ and capillary number $Ca \sim \mathcal{O}(10^{-2})$. Due to low value of the Ca, we are in the regime where deformation of the interface can be neglected.

We consider a density matched system, thus the gravitational Bond number

$$\mathrm{Bo} = (\rho_p - \rho_1) g R^2/\sigma = 0. \tag{15}$$

An additional non-dimensional measure associated with interface thickness is given by Cahn number,

$$\mathrm{Cn} = \frac{\chi}{R} \tag{16}$$

In the current study, Cn is fixed at a constant value of 0.15.

III. Results and Discussion

A. Contact angle validation

Depending the wetting of the particle surface, the colloid is displaced vertically with respect to the interface (Fig. 2). This allows the measurement of the contact angle θ using equation 10. In Fig. 2(a) the influence of wetting parameter h on the contact angle observed from the simulations is compared with the theoretical values. The simulations are in good agreement with the theoretical estimation for $\theta \in [60°, 120°]$. However, a deviation from the theoretical prediction is observed towards the two extremes $h = \pm 0.4$ (Fig. 2(a)). This deviation probably arises due to the discretisation of the particle surface on the lattice. We have thus limited our range between $\theta \sim 108°$ and $\theta \sim 72°$ respectively as upper and lower limit for θ in the simulations of the particle dynamics.

B. Drag on a neutrally wetting colloid

To validate our simulation method, we conducted a numerical experiment with a neutrally wetting colloidal particle ($\theta = 90°$) dragged along the fluid-fluid interface with a viscosity ratio $\lambda = 1$ (Fig. 2c).

Under Stokes flow, the drag force on a translating spherical particle in the bulk fluid is given by,

$$F = 6\pi\eta R V \tag{17}$$

where η is the viscosity of the fluid, R is the radius of the particle and V is its velocity. By varying F, we find a linear force-velocity relation as expected from Stokes's law (Fig. 3).

Since our domain size is finite and we used periodic boundary conditions our drag coefficient would be af-

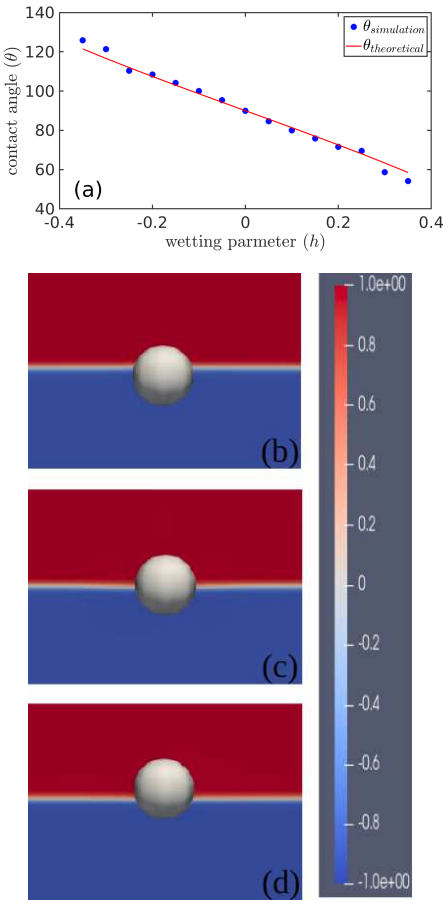

FIG. 2. (a) Contact angle versus wetting parameter defined as $h = H\sqrt{\frac{1}{\kappa B}}$ for the case of viscosity ratio $\lambda = 1.0$. Blue circles are the values obtained from the simulation using Eq. 10 and red line is from theoretical calculation using Eq. 11. Different values of colloidal contact angles measured at the interface. (b-d) Snapshots from the simulations for different contact angles: (b) $\theta \approx 72°$, (c) $\theta \approx 90°$ and (d) $\theta \approx 108°$. Red colour corresponds to $\phi = +1$ and and blue to $\phi = -1$ fluids with viscosities η_1 and η_2, respectively.

fected by finite size effects. To correct for these, we use a correction by Hasimoto[32] derived for the Stokes' drag of a periodic array of spherical particles. For the case of simple cubic arrangement, corresponding a single colloid in a cubic box with periodic boundary conditions, the

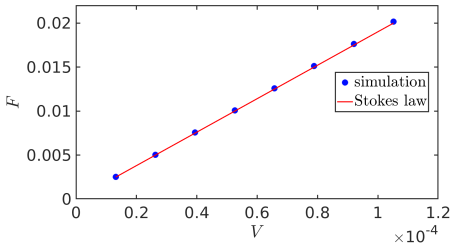

FIG. 3. The force-velocity characteristics for the colloidal particle of radius $R = 12.0$ at the interface with contact angle $\theta = 90°$ and viscosity ratio $\lambda = 1.0$. The simulation data is fitted with Stokes drag (Eq. 17) of a spherical particle and includes Hashimoto[32] correction parameter Q Eq. 18 (see the text for more details).

correction is given by[32]

$$Q = 1 - 1.7601\sqrt[3]{C_\tau} + C_\tau - 1.5593C_\tau^2 \qquad (18)$$

$$C_\tau = \frac{4\pi}{3}\frac{R^3}{L^3} \qquad (19)$$

where C_τ is the volume fraction, L is the box length.

Using the correction, we recover an excellent agreement between the simulations and the Stokes' result (Eq. 17) for a neutrally wetting colloid at an interface with $\lambda = 1$ (Fig. 3).

C. Translation dynamics: the effect of the viscosity ratio and a contact angle

The main aim of this work is to study the hydrodynamic drag of a spherical colloidal particle trapped at an interface between two fluids. The drag coefficient is determined as the function of the viscosity contrast $\lambda = \eta_2/\eta_1$ and the contact angle θ. To investigate the translational dynamics, the particle was pulled along the interface by a constant force $F = 0.01125$. After initial transient, the particle velocity was averaged over the last 1×10^5 steps in the steady state.

For a contact angle different from 90° or for a viscosity ratio different from 1, the drag on the upper and lower hemispheres differs, resulting in a torque around an axis perpendicular on the interface normal and the direction of the translational velocity V. The resulting translation-rotation coupling leads to a superposition of gliding and rolling motion with a finite angular velocity Ω, as discussed in more detail in the section III D. Further, we consider the case where the rotation is inhibited and find a velocity $\hat{V}$ which in general differs from V.

In Fig. 4(a) we plot both V and $\hat{V}$ as a function of $\epsilon = \cos\theta$, for various values of the viscosity ratio λ. The

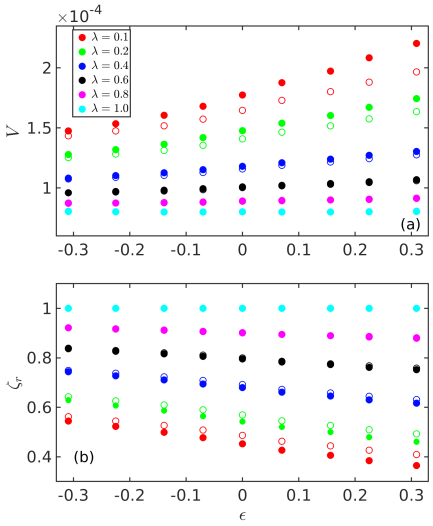

FIG. 4. (a) Velocity versus $\epsilon = \cos\theta$ for different values of the viscosity ratio λ. Closed and open symbols correspond to observed velocities with V and without rotation $\hat{V}$, respectively. (b) The effective drag coefficient ratio ζ_r and $\hat{\zeta}_r$, as defined in Eq. (20).

velocity shows a roughly linear variation with ϵ and decreases with increasing viscosity ratio λ. Both dependencies are qualitatively understood when noting that $\cos\theta$ provides a measure of the fraction of the particle volume immersed in the less viscous fluid, and that $1+\lambda$ accounts for the mean viscosity of the two fluids in the units of η_1.

Regarding the effect of the rolling motion, we find that the velocity of rotating particles is in general larger, $V > \hat{V}$, and that this effect increases with ϵ yet decreases with λ. These dependencies are readily understood from the data in Fig. 4: The overall reduction of the viscous stress due to the rotation is most efficient for a large volume fraction immersed in the low-viscosity fluid (large ϵ) and for a large viscosity contrast (small λ).

The drag coefficient $\zeta = F/V$ of a freely rotating particle is given by the ratio of the applied force F and the velocity V; we also define a reduced drag coefficient

$$\zeta_r = \frac{\zeta(\lambda)}{\zeta(1)}. \tag{20}$$

Similarly we define $\hat{\zeta}$ and $\hat{\zeta}_r$ when the particle rotation is inhibited. The drag ratio ζ_r is plotted against contact angle for different values of the viscosity ratio λ in Fig. 4(b). We find that at constant ϵ, the drag increases with increasing viscosity ratio λ. At constant $\lambda < 0$, the drag increases with the immersion parameter ϵ, that is, with the fraction of the particle volume immersed in the high-viscosity phase, in agreement with the previous studies[19–22,33].

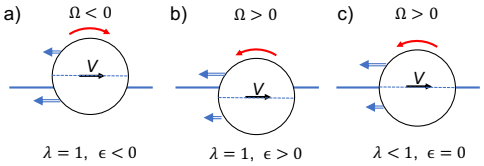

FIG. 5. Schematic view of translation-rotation coupling of a particle moving at velocity V to the right. (a) The viscosity is the same above and below the interface, $\lambda = 1$, wheres the large contact angle $\theta > 90^\circ$ implies $\epsilon < 0$. Because of the additional viscous stress at the contact line, the drag force on the lower hemisphere is larger than on the upper one, as indicated by double arrows, resulting in a clockwise rotation of the particle. (b) For a small contact angle $\theta < 90^\circ$, the contact line is on upper hemisphere, and the particle rotates counter-clockwise. (c) The viscosity in the upper halfspace is larger than in the lower, $\lambda < 1$. The larger viscous drag on the upper hemisphere favors counter-clockwise rotation.

D. Rotational dynamics

The hydrodynamic drag forces on the upper and lower hemispheres differ in general, thus exerting a torque which results in a steady-state rotation of the particle, as shown schematically in Fig. 5. We calculated the angular velocity Ω of the colloid using the same averaging procedure as the calculation of V.

In Fig. 6 we plot Ω as a function of the immersion parameter $\epsilon = \cos\theta$ for different values of the viscosity ratio λ. For identical viscosities, $\lambda = 1$, the angular velocity is small and roughly linear in ϵ. The sign of Ω is readily understood when noting that the interface position with respect to the particle center reads $R\epsilon$. Close to the contact line the flow field is strongly perturbed by the presence of the interface, thus engendering additional viscous stress and enhancing the backward drag force on the lower hemisphere in Fig. 5a and on the upper hemisphere in Fig. 5b. As a consequence, the particle rotates clockwise in (a) and counter-clockwise in (b).

Much larger values of Ω occur for a finite viscosity contrast between the two fluids. In our simulations $\lambda < 1$ indicates higher viscosity in the upper halfspace, such that the backward drag force is larger on the upper hemisphere and the particle rotates counterclockwise (Fig. 5c). In the case $\lambda < 1$ and $\epsilon < 0$, the mechanisms (a) and (c) partly cancel each other. The data in Fig. 6 show that the viscosity ratio has a stronger effect; for $\lambda < 0.8$ the angular velocity is positive, even for negative ϵ.

Das et. al.[22] considered spherical neutrally wetting particles straddling on a liquid film on a solid surface. Our value $\Omega R/V = 0.206$ for $\lambda = 0.1$ and $\epsilon = 0$, differs

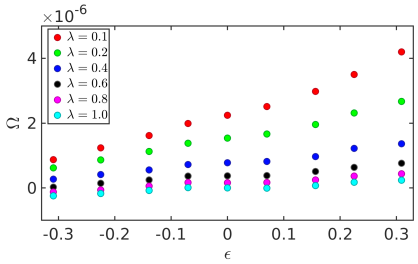

FIG. 6. The angular velocity of the colloid Ω versus cosine of contact angle $\epsilon = \cos\theta$ for different values of the viscosity ratio λ.

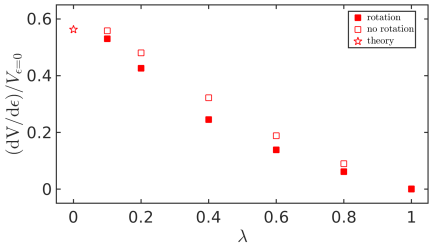

FIG. 7. Velocity derivative taken with respective to ϵ in the close neighbourhood around $\epsilon = 0$, where linear approximation is valid (slopes from Fig. 4(a) normalized with colloid velocity at $\epsilon = 0$ at corresponding λ value. Open star corresponds to theory (Eq. 21); closed squares correspond to case with rotation and open squares correspond to without rotation of the colloid.

by less than 2% from $\Omega R/V = 0.21$ calculated by Das et. al.[22] for $\lambda = 0$ and $\epsilon = 0$ at large film depth. At present it is not clear whether this tiny discrepancy arises from the difference in λ or to the fact that Das et al. consider an ideal interface (see below).

E. Comparison with theory

Our simulations for non-rotating particles are largely motivated by the existence of theoretical predictions for particles moving along an ideally thin and stiff interface. Regarding the dependence on the contact angle, we compare our findings for the velocity $\hat{V}$ with the perturbative expression for the drag force at a gas-liquid interface ($\lambda = 0$), first derived by Brenner[34] and reinterpreted by Dörr and Hardt[35],

$$F = 3\pi\eta_1 R\hat{V}\left(1 - \frac{9}{16}\cos\theta + ...\right). \tag{21}$$

This formula is exact to linear order in ϵ; for $\epsilon = 0$ it reduces to half of the Stokes drag in a bulk liquid. Solving for $\hat{V}$ and taking the derivative with respect to ϵ we find

$$\frac{1}{\hat{V}}\frac{d\hat{V}}{d\epsilon}\bigg|_{\epsilon=0} = \frac{9}{16} \quad (\lambda = 0). \tag{22}$$

In Fig. 7 we show this derivative obtained from our simulation as a function of λ. As expected the derivative vanishes at $\lambda = 1$ and increases for smaller values of λ, that is, for increasing viscosity contrast. The simulation data at small λ agree almost quantitatively with the theoretical result (22), indicated as an open star. Still, extrapolating our data to $\lambda = 0$ would suggest a derivative slightly larger than the value $\frac{9}{16}$ expected for an ideally thin and stiff interface.

Now we turn to the dependence of the drag on a neutrally wetting particle as a function of the viscosity ratio, which has been derived by Pozrikidis[20],

$$F = 3\pi\eta_1 R\hat{V}(1+\lambda), \quad (\epsilon = 0). \tag{23}$$

The corresponding drag ratio reads as

$$\hat{\zeta}_r = \frac{1+\lambda}{2}, \quad (\epsilon = 0). \tag{24}$$

For $\lambda = 1$ this corresponds to a bulk fluid, whereas for $\lambda = 0$ it represents a gas-liquid interface, where the drag force is half of the bulk value. In Fig. 8 we compare the drag ratio obtained from our simulation data for $\epsilon = 0$ with Pozrikidis's result. For viscosity ratios $\lambda > \frac{1}{2}$ we find a good agreement. For smaller values, however, our simulation shows a lower drag ratio than expected from theory for interfaces of zero thickness and infinite capillary number. In the limit $\lambda \to 0$ the simulation data for $\hat{\zeta}_r$ (open circles) clearly do not converge toward $\frac{1}{2}$ but toward a significantly smaller value below 0.4. This effect occurs for both rotating and non-rotating particles, though it is slightly larger for the former.

Furthermore, we also present the simulation data of Das et al.[22] (open and closed stars) for an ideal gas-liquid interface ($\lambda = 0$). Their data for a non-rotating particle (open star) is in excellent agreement with Pozrikidis's data, whereas the drag ratio for a rotating particle (closed star) is reduced by about ten percent. This reduction in the drag ratio for rotating particles compares well with the findings at small λ of the present work.

To rationalize the deviation of our data for the drag ratio ζ_r from theory, we remind that our simulations are done for a Cahn-Hilliard diffuse interface of a finite width and a finite surface tension, whereas the theory results, eqs. (22) and (24), and the data of Das et al. are obtained for an an ideal interface of infinite tension and zero width. In the view of the rather small capillary number used in our simulations, Ca = 0.01, the strong

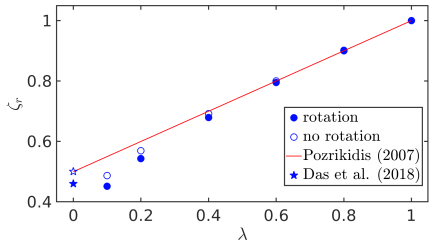

FIG. 8. Comparison of non-dimensional drag ratio (ζ_r) given in Eq. 20 for the colloidal particle at fluid-fluid interface with contact angle $\epsilon = 0$ for different values of viscosity ratio (λ) with Refs.[20,22]. Here circles are from the simulations, closed and open stars correspond to Das et. al.[22] with and without particle rotation. The solid line is obtained from a theoretical estimation given by Eq. 23.

discrepancy shown visible in Fig. 8 can hardly be related to deformation of the interface. This suggest that the observed deviations may stem from the finite interfacial width, and could be related to a decoupling of the thermodynamic and hydrodynamic interfaces, defined by zero composition variable $\phi = 0$ and zero normal velocity $v_\perp = 0$, respectively.

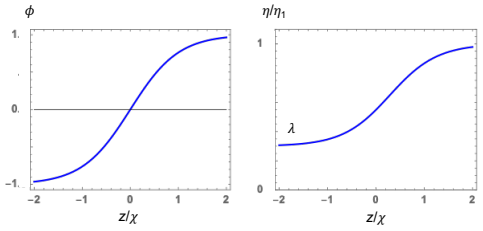

FIG. 9. Phase and viscosity variation through the interface, with the length scale χ defined in (2).

In the steady-state and for small Reynolds number, the Navier-Stokes equation (5) simplifies to

$$\eta\nabla^2\mathbf{v} - \nabla P - \phi\nabla\mu = 0. \tag{25}$$

At the thermodynamic definition for the interface, $\phi = 0$, the last term vanishes. Yet there does not seem to be an obvious argument why the vertical velocity should vanish at the surface defined by $\phi = 0$. In Fig. 9 we plot the phase ϕ and the viscosity η across the interface. Both vary smoothly at the scale of the interface width χ, and so does the stress term in (25). Intuitively one would expect that, in order to minimize the overall dissipation, the flow field becomes smoother in the more viscous fluid above the interface, and that the sharp velocity changes required at the contact line rather occur in the less viscous phase. This would imply an asymmetric flow profile in the vicinity of the surface $\phi = 0$, and an overall reduction of dissipation with respect to the ideal interface of zero thickness. This could explain our observation of the reduced drag coefficient shown in Fig. 8. The spatial resolution of the interface in our simulations was not sufficient to provide unambiguous data on the flow profile within and close to the surface $\phi = 0$. In future studies, this could improved by increasing the interfacial width χ.

IV. Conclusions

In summary, we studied the dynamics of a spherical colloidal particle at fluid-fluid interface using Lattice-Boltzmann Method (LBM). Our simulations include the effects of interfacial thermodynamics and particle wetting, in addition to the hydrodynamics. The translational and angular velocities of the particle were analysed both as the function of the viscosity ratio λ between the two fluids, and the contact angle θ between the fluids and the colloidal surface.

Our results are in overall good agreement with previous hydrodynamic theories. The drag is reduced when the particle prefers thermodynamically a position where its surface is more in the low viscosity fluid. Further, the viscosity contrast leads to a rotational motion of the particle. The effect of the rotation was analysed by applying a strong aligning field, which stops the rotation and slighlty increases the hydrodynamic drag. Comparison with theoretical findings and previous simulations for ideally thin and stiff interfaces, reveals a discrepancy in the drag coefficient, which could be related to the finite width of the interface considered here.

Acknowledgements

HG would like to thank Dr. Zaiyi Shen and Sotiris Samatas for engaging and helpful discussions. HG and JSL acknowledge IdEx (Initiative d'Excellence) Bordeaux for funding, Curta cluster for computational time. JSL acknowledges support by the French National Research Agency (ANR) project GASPP through Contract No. ANR-19-CE06-0012-01. AW acknowledges support through contract No. ANR-19-CE30-0012-01

Appendix

Domain and grid independence

The simulations were initialised with a fully separated binary fluid mixture with a well-defined interface between the fluids following an equilibrium profile (Eq. 3). A colloidal particle is placed at the interface, and a constant pulling force F is applied along the interface. The accu-

racy of the numerical results is sensitive to choice of both size of the simulation box (L) and particle radius (R). Table I shows the domain independence study on drag force calculations with particle radius $R = 12$, viscosity ratio $\lambda = 1.0$ and contact angle $\theta = 90^\circ$ using three values of domain sizes 108, 128 and 160. It is evident from the table that, increasing the domain size from 128 to 160, there is a negligible change ($< 1\%$) in the value of drag force value. Since the error is under an acceptable limit, we have used domain size of $128 \times 128 \times 128$ in all our simulations to reduce the computational cost.

Domain size	$error\%$
108	1.1423
128	0.7061
160	0.4424

TABLE I. Relative error in drag force measurement from simulations and theory (Eq.17) of a particle with radius $R = 12$, contact angle $\theta = 90^\circ$ and viscosity ratio $\lambda = 1$ for different domain sizes.

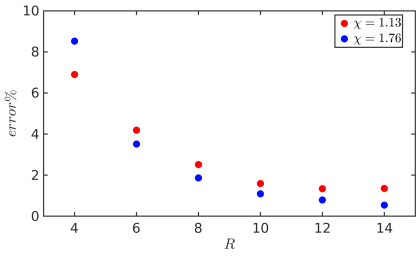

FIG. 10. Error percentage between drag force obtained from simulation and theory (Eq. 23) for different values particle radius (R) and interfacial thickness (χ). Simulations were carried out using a periodic simulation domain $128\times128\times128$.

After fixing the domain size at a satisfactory value, it is also important to find satisfactory size of the particle. Fig. 10, shows the deviation from the theoretical drag force calculation for different particle sizes with viscosity ratio $\lambda = 1.0$ and contact angle $\theta = 90^\circ$ using two values of interfacial widths $\chi = 1.13, 1.76$. The error percentage is small ($< 2\%$) for the particle sizes $10, 12$ and 14 with $\chi = 1.76$. We have chosen the colloid radius $R = 12$ and interfacial width $\chi = 1.76$ in the present work.

DATA AVAILABILITY

The data that support the findings of this study are available from the corresponding author upon reasonable request.

[1] A. D. Dinsmore, M. F. Hsu, M. G. Nikolaides, M. Marquez, A. R. Bausch, and D. A. Weitz, "Colloidosomes: Selectively permeable capsules composed of colloidal particles," Science **298**, 1006–1009 (2002).
[2] R. Aveyard, B. P. Binks, and J. H. Clint, "Emulsions stabilised solely by colloidal particles," Advances in Colloid and Interface Science **100**, 503–546 (2003).
[3] P. S. Clegg, E. M. Herzig, A. B. Schofield, T. S. Horozov, B. P. Binks, M. E. Cates, and W. C. K. Poon, "Colloid-stabilized emulsions: behaviour as the interfacial tension is reduced," Journal of Physics: Condensed Matter **17**, 3433–3438 (2005).
[4] T. S. Horozov, "Foams and foam films stabilised by solid particles," Current Opinion in Colloid and Interface Science **13**, 134–140 (2008).
[5] S. Lam, K. P. Velikov, and O. D. Velev, "Pickering stabilization of foams and emulsions with particles of biological origin," Current Opinion in Colloid & Interface Science **19**, 490–500 (2014).
[6] M. E. Cates and P. S. Clegg, "Bijels: a new class of soft materials," Soft Matter **4**, 2132–2138 (2008).
[7] K. Stratford, R. Adhikari, I. Pagonabarraga, J.-C. Desplat, and M. E. Cates, "Colloidal jamming at interfaces: A route to fluid-bicontinuous gels," Science **309**, 2198–2201 (2005).
[8] S. Aland, J. Lowengrub, and A. Voigt, "A continuum model of colloid-stabilized interfaces," Physics of Fluids **23**, 062103 (2011).
[9] R. Arabjamaloei, R. S. Shah, S. Bryant, and M. Trifkovic, "Controlling structure of materials derived from spinodally decomposing liquids," Physics of Fluids **33**, 032020 (2021).
[10] P. S. Bhosale, M. V. Panchagnula, and H. A. Stretz, "Mechanically robust nanoparticle stabilized transparent liquid marbles," Applied Physics Letters **93**, 034109 (2008).
[11] N. Janardan, M. V. Panchagnula, and E. Bormashenko, "Liquid marbles: Physics and applications," Sadhana **40**, 653–671 (2015).
[12] W. Ramsden, "Separation of solids in the surface-layers of solutions and 'suspensions' (observations on surface-membranes, bubbles, emulsions, and mechanical coagulation," Proc. R. Soc. Lond. **72**, 156–164 (1903).
[13] S. U. Pickering, "Cxcvi.—emulsions," J. Chem. Soc., Trans. **91**, 2001–2021 (1907).
[14] B. Radoev, M. Nedyalkov, and V. Dyakovich, "Brownian motion at liquid-gas interfaces. 1. diffusion coefficients of macroparticles at pure interfaces," Langmuir **8**, 2962–2965 (1992).
[15] J. T. Petkov, N. D. Denkov, K. D. Danov, O. D. Velev, R. Aust, and F. Durst, "Measurement of the drag coefficient of spherical particles attached to fluid interfaces," Journal of Colloid and Interface Science **172**, 147–154 (1995).
[16] R. B. Walder, A. Honciuc, and D. K. Schwartz, "Phospholipid diffusion at the oilwater interface," Journal of Physical Chemistry B **114**, 11484–11488 (2010).
[17] D. Wang, S. Yordanov, H. M. Paroor, A. Mukhopadhyay, C. Y. Li, H. J. Butt, and K. Koynov, "Probing diffusion of single nanoparticles at water–oil interfaces," Small **7**, 3502–3507 (2011).
[18] I. Sriram, R. Walder, and D. K. Schwartz, "Stokes–einstein and desorption-mediated diffusion of protein molecules at the oil–water interface," Soft Matter **8**, 6000 (2012).
[19] K. Danov, R. Aust, F. Durst, and U. Lange, "Influence of the surface viscosity on the hydrodynamic resistance and surface diffusivity of a large brownian particle," Journal of Colloid and Interface Science **175**, 36–45 (1995).
[20] C. Pozrikidis, "Particle motion near and inside an interface," Journal of Fluid Mechanics **575**, 333–357 (2007).
[21] A. Dörr, S. Hardt, H. Masoud, and H. A. Stone, "Drag and diffusion coefficients of a spherical particle attached to a fluid–fluid interface," Journal of Fluid Mechanics **790**, 607–618 (2016).
[22] S. Das, J. Koplik, R. Farinato, D. R. Nagaraj, C. Maldarelli, and P. Somasundaran, "The translational and rotational dynamics of a colloid moving along the air-liquid interface of a thin film," Scientific Reports **8**, 8910 (2018).
[23] J. C. Loudet, M. Qiu, J. Hemauer, and J. J. Feng, "Drag force on a particle straddling a fluid interface: Influence of interfacial deformations," The European Physical Journal E **43**, 1–13

(2020).
[24]G. Lecrivain, R. Yamamoto, U. Hampel, and T. Taniguchi, "Direct numerical simulation of a particle attachment to an immersed bubble," Physics of Fluids **28**, 083301 (2016).
[25]A. Gaddam, A. Agrawal, S. S. Joshi, and M. C. Thompson, "Slippage on a particle-laden liquid-gas interface in textured microchannels," Physics of Fluids **30**, 032101 (2018).
[26]V. M. Kendon, M. E. Cates, I. Pagonabarraga, and J. Desplat, "Inertial effects in three dimensional spinodal decomposition of a symmetric binary fluid mixture: A lattice boltzmann study," Journal of Fluid Mechanics **440**, 147–203 (2001).
[27]J.-C. Desplat, I. Pagonabarraga, and P. Bladon, "Ludwig: A parallel lattice-boltzmann code for complex fluids," Computer Physics Communications **134**, 273–290 (2001).
[28]K. S. et al., "ludwig: v0.11.0," (2020), see https://github.com/ludwig-cf/ludwig.
[29]A. J. C. Ladd, "Numerical simulations of particulate suspensions via a discretized boltzmann equation. part 1. theoretical foundation," Journal of Fluid Mechanics **271**, 285 (1994).
[30]A. J. C. Ladd, "Numerical simulations of particulate suspensions via a discretized boltzmann equation. part 2. numerical results," Journal of Fluid Mechanics **271**, 311 (1994).
[31]K. Langaas and J. Yeomans, "Lattice boltzmann simulation of a binary fluid with different phase viscosities and its application to fingering in two dimensions," The European Physical Journal B **15**, 133–141 (2000).
[32]H. Hasimoto., "On the periodic fundamental solutions of the stokes equations and their application to viscous flow past a cubic array of spheres," Journal of Fluid Mechanics **5**, 317–328 (1959).
[33]T. M. Fischer, P. Dhar, and Heinig, "The viscous drag of spheres and filaments moving in membranes or monolayers," Journal of Fluid Mechanics **558**, 451–475 (2006).
[34]H. Brenner, "The stokes resistance of a slightly deformed sphere." Chemical Engineering Science **19**, 519–539 (1964).
[35]A. Dörr and S. Hardt, "Driven particles at fluid interfaces acting as capillary dipoles," Journal of Fluid Mechanics **770**, 5–26 (2015).